Simulation-assisted investigation on the formation of layer bands and the microstructural evolution in directed energy deposition of Ti6Al4V blocks

Article *in* Virtual and Physical Prototyping · June 2021

DOI: 10.1080/17452759.2021.1942077

8 authors, including:

Xufei Lu
Universitat Politècnica de Catalunya
28 PUBLICATIONS **351** CITATIONS
SEE PROFILE

Guohao Zhang
Northwestern Polytechnical University
7 PUBLICATIONS **67** CITATIONS
SEE PROFILE

Miguel Cervera
Universitat Politècnica de Catalunya
408 PUBLICATIONS **7,670** CITATIONS
SEE PROFILE

Michele Chiumenti
Universitat Politècnica de Catalunya
276 PUBLICATIONS **3,831** CITATIONS
SEE PROFILE

Simulation-assisted investigation on the formation of layer bands and the microstructural evolution in directed energy deposition of Ti6Al4V blocks

Abstract: Directed energy deposition of titanium alloy entails severe microstructural heterogeneity and layer bands due to diverse thermal histories. While the thermal-microstructure relationship in additive manufacturing has been reported, the details on how complex thermal histories influence the microstructural features and evolution have not been so addressed, and the mechanism of the band formation in multi-layer multi-pass builds is still unclear. To undertake such investigation, a thermal model is firstly calibrated using two part-scale Ti6Al4V blocks fabricated on differently sized substrates, and then used to study the relationship between key microstructural characteristics and the thermal cycling involved. Results show that the different evolutions of the temperature ranges just underneath the β-transus temperature (T_β) controlled by the printing path are responsible for the different band distributions at the center and corner of the blocks. Also, the α sizes in the normal region are closely linked to the integral area obtained from the thermal curve as temperature fluctuates between T_β and α dissolution temperature, which helps linking the processing variables to metallurgy. This further demonstrates that the α coarsening during thermal cycles is primarily driven by multi dissolution and precipation transformations instead of Ostwald ripening. Finally, the quantitative thermal-microstructure-microhardness relationship is established, this being helpful for the microstructural design.

Keywords: Directed energy deposition; Additive manufacturing; Microstructural evolution; Layer bands; Thermal simulation; Ti6Al4V blocks.

1. Introduction

Metal Additive Manufacturing (AM) is an advanced layer-by-layer fabrication technology that is revolutionizing the conventional manufacturing industry due to the capability to produce more complex structures, achieving the reduction of material waste, part weight and assembly complexity (Baiges et al. 2021; Goh et al. 2021). Compared to other AM techniques such as Selective Laser Melting (SLM) (Zhang et al. 2020), Directed Energy Deposition (DED) has a higher deposition efficiency, suitable for fabricating larger structural parts (Tang et al. 2020). In DED processes the metal powder is concentrically blown into the molten pool induced by a high-energy laser beam moving according to user-defined building sequences (Lu et al. 2019).

The Ti6Al4V titanium alloy is one kind of common AM alloys widely employed for aircraft structural components due to its low density, high fracture toughness, high strength and excellent corrosion properties (Wang et al. 2019). Typical microstructures of AM Ti6Al4V are mainly comprised of basketweave α, colony structure, massive αm and martensite α′ (Ren et al. 2017; Fan et al. 2018), depending on the specific temperature history in the printing process (Zhao et al. 2017).

In AM processes, the microstructure in one sample is hardly the same at different deposition positions even if the process parameters are kept constant, due to the discrepancy in the thermal histories. For instance, regularly distributed microstructural bands are usually observed in Ti-6Al-4V workpieces fabricated by different AM methods (Sandgren et al. 2016; Qiu et al, 2015). Kobryn and Semiatin 2003 first reported layer bands in DED titanium alloy induced by re-heating of the baseplate materials to the β-transus temperature (T_β). Kelly and Kampe 2004 suggested that a particular combination of peak temperature (reached in the zone where the α volume fraction starts to decline), duration of the peak temperature and the cooling rate during

thermal cycling is responsible for the formation of bands in Ti6Al4V single-wall parts fabricated by DED. Recently, Ho et al. 2019 carried out a thermal simulation to analyse the microstructural bands in Ti6Al4V single-wall pieces fabricated by wire-arc additive manufacturing (WAAM) and demonstrated that the thin colony morphology white area at the band top is caused by a peak temperature increase just below T_β during thermal cycles. The layer bands in most single-wall samples usually have a regular spacing equivalent to the layer-thickness because of the use of the simplex printing path, but this is not the case in the multi-layer multi-pass blocks. Here, the intersecting building sequence is used to fabricate the blocks, and the increasing complexity of the thermal history induced by the building process leads to dissimilar band distributions. This phenomenon has not been previously investigated.

In addition to the formation of layer bands, the microstructure in the regions without bands is also strongly dependent on the thermal history experienced, considerably influenced by the process parameters, scanning pattern, part size and geometry, preheating and material properties. Numerous studies have focused on the relationship between the AM variables, thermal history and microstructure (Zhao et al. 2020). Qian et al. 2005 found that increasing the laser power strengthens the thermal effect, contributing to a pronounced coarsening of α structure and the appearance of colony morphology in Ti6Al4V build by DED. Crespo and Vilar 2010 coupled thermal modelling and phase transformation kinetics as well as relations between microstructure and mechanical properties such as Young's modulus and hardness to generate processing maps for DED Ti6Al4V. Their results show that the microstructure is determined by the cooling rate, influenced by the scanning speed and idle time. Kürnsteiner et al. 2020 achieved a pronounced improvement of the mechanical properties of AM parts by controlling the repeated thermal cycles (so-called intrinsic

heat treatment (IHT)) to tailor the microstructure. Zhang et al. 2021 obtained in-situ grain refinement of commercially pure-titanium through properly increasing the input energy density to affect the cyclic re-heating inherent to the SLM process.

Even though the thermal history in AM has been directly or indirectly used to study and further optimize the microstructure and mechanical properties of the build, a deeper understanding on the intrinsic relationship between them is still missing and further quantitative evaluation on the thermal and microstructural responses is needed. In AM, the final microstructure is strikingly different from the first one formed under a sharp cooling rate (10^3 °C/s for DED (Wolff et al. 2017)) on account of the repeated thermal cycles (as the IHT effect), especially in the lower part of the deposited block. Likely, only the latter part of the thermal history in the AM process (where peak temperature is below T_β) is responsible for the final microstructure, but the details are currently poorly understood. Also, the combined effect of the thermal cycling in the range between T_β and α dissolution temperatures (T_{diss}) and the acting-time involved on the microstructural development has not been sufficiently studied.

Numerical simulation is a powerful tool to study the complex physical problems induced by AM processes (Li et al. 2018; Tan et al. 2020). In previous works, an in-house 3D finite element (FE) software has been used for the accurate thermo-mechanical response during and after the AM process, but the coupling with microstructure was not investigated (Chiumenti et al. 2017; Lu et al. 2018). Tan et al. 2019 developed a temperature driven phase-transformation model to predict the phase volume fraction of Ti6Al4V by SLM. Li et al. 2017 also coupled the heat transfer with phase transition during SLM process to better capture the physics near the melting pool. While most of the modelling works on microstructure to date are focused on small

parts such as single-tracks (Liu et al. 2021; Zhang et al. 2021), the metallurgical prediction in part-scale AM builds is still challenging.

Based on the above analyses, this work aims to elucidate the formation mechanism of layer bands and to quantitatively study the relation between key microstructural characteristics and the thermal history in Ti6Al4V multi-layer multi-pass blocks by DED. Firstly, the thermal model is calibrated using in-situ temperature measurements from two 40-layers blocks deposited on differently sized baseplates. Next, the predicted temperature data are used to investigate the different band distributions observed and the coarsening of α-lamellar in DED blocks. Finally, the quantitative relationship between thermal history, microstructure and microhardness is formulated.

2. Experiment and Simulation

To date, several researchers have reported on the influence of the process parameters on the microstructure of AM parts (Kou et al. 2020; Liu et al. 2011). However, the effect of the substrate has rarely been investigated. In this work, two differently sized substrates are studied to evaluate their respective thermal and metallurgical evolutions. An alternating scanning path is used to produce distinct thermal histories and to allow the comparative study on the formation of layer bands and the thermal-microstructure relationship.

2.1. Experiment procedure

Two block parts were constructed by a DED system consisting of a semiconductor laser diode with a maximum power of 6 kW, a DPSF-2 high precision adjustable automatic powder feeder, a five-axis numerical control working table and an argon purged processing chamber with low oxygen content. Spherical Ti6Al4V powder with 53~150 μm diameter and low oxygen (below 0.12 wt%) was used as the deposition

material. Before the DED experiments, the powder was dried in a vacuum oven for 2.5 h at 130°C to remove the moisture absorption.

Two annealed Ti6Al4V baseplates with different geometric dimensions were used as shown in Figure 1. The plate sizes and the clamping conditions are as follow: (i) small substrate: 140×50×6 mm^3, fixed as a bridge; and (ii) large substrate: 200×100×25 mm^3, clamped as a cantilever. Figure 1 also shows the locations (points CH1 to CH6) of the thermocouples used to in-situ measure the temperature evolution of the bottom surface of the baseplates. Six Omega GG-K-30 type-K thermocouples with a measurement uncertainty of 2.2°C are employed and the temperature signal is collected by a Graphtec GL-900 8 high-speed data-logger.

Figure 2 shows the building strategy with 4 different sequences looped every 4-layers. The DED process parameters used to build the 40-layers blocks with a size of 125×35×20 mm^3 are given Table 1.

For microstructure observation the DED samples are firstly sectioned in the XZ plane by machining and then polished. A chemical solution consisting of 3 ml HNO_3, 1 ml HF and 46 ml H_2O is used as etching agent. Next, the microstructures of Ti6Al4V fabricated by DED are characterized by optical microscopy (Keyence VH-Z50L). Imaging Pro Plus 6 software is employed to measure the sizes of the α lamellar from six photographs with a magnification of 2000 in each sample. Each α plate is measured at least three times at different locations (middle and two ends) and the measured number of all α laths exceeds 100 in each sample. Finally, the mean value of the observed sizes is calculated. Additionally, the Vickers hardness is determined by a Duranmin-A300 micro-hardness tester. Ten different points are selected to measure in each deposition position. The measurements are performed with a load of 2000 g and a load time of 15 s.

2.2. Thermal simulation

In this work, an in-house FE software platform, COMET, is used to perform the high-fidelity simulation of the full-field temperature during the DED process (Chiumenti et al. 2010; Cervera, Saracibar, and Chiumenti 2002). The 3D modelling, the FE-mesh generation and the pre/post-processing are all carried out via the GiD pre-post-processor (García, García, and Gómez 2010). A more detailed description of this thermal model can be found in previous works (Chiumenti et al. 2016; Lu et al. 2021). Two assumptions are adopted: (i) the latent heat is not considered, because the heat absorbed during solid to liquid transformation and the heat release during solidification is exactly the same; (ii) the heat due to plastic deformation is negligible if compared to the laser input.

Figure 3(a) shows the FE models of the printed blocks deposited on two plates with different dimensions: (i) the small one including 141,104 hexahedral elements and 151,180 nodes, and (ii) the large one consisting of 142,576 elements and 153,320 nodes. The size of the deposited elements is set as 1.25×1.25×0.5 mm^3, based on the grid sensitivity analyses (Chiumenti et al. 2017). The mesh in the base is gradually coarsened far away from the deposit. Figure 3(b) schematically illustrates the locations to sample the thermal history and the experimental microstructure. The positions corresponding to the centre and corner of the small and large substrates are named as Case S0, Case S1, Case L0 and L1, respectively.

Both the metal deposition and the baseplate are assumed to be thermally isotropic and to have the same thermal physical properties as the Ti6Al4V alloy, listed in Table 2 (Lu et al. 2019). During the thermal analysis for DED, heat transfer by radiation and convection between the workpiece and its surrounding is considered in all the external surfaces of both the build and the baseplate; a convective heat transfer coefficient

(HTC) of 5 W/(m^2·ºC) and an emissivity of 0.45 are set. A higher HTC of 40 W/(m^2·ºC) is used to model the thermal interface between the clamp and the baseplate. The ambient temperature is fixed at $T_{room} = 24°C$. Laser energy efficiency for the DED process is set at 0.37. To guarantee accuracy of the simulation, all the model parameters used in this work were determined by matching the numerical thermal histories with in-situ measurements.

3. Results

3.1. Model calibration and thermal history

To calibrate the FE model for the DED process, the calculated temperature histories of two workpieces are compared with the in-situ experimental measurements, as shown in Figure 4. Remarkable agreement is obtained between the computed and experimental data. It can be seen that the computed thermal curves (solid lines) agree well with the experimental results (dash lines) at all six sampling points. The very slight difference between them is caused by the simplification of the thermal boundary conditions (e.g. convection and emissivity). Table 3 shows the average error in the whole simulation for each case. The maximum does not exceed 2.77%. This successful calibration of the model indicates that it can be employed to accurately predict the thermal history that the build experiences during the DED process.

Figure 5 presents the thermal history of the points located at the bottom, middle and top of the deposited blocks in different cases. These positions correspond to the building heights of 0.5 mm (1^{st} layer), 10 mm (20^{th} layer) and 19.5 mm (40^{th} layer), respectively, as shown in Figure 3(b). On the whole, all thermal curves present a decreasing peak temperature with similar fluctuation, while the average temperature for the different cases differs due to the pronounced differences on the thermal accumulation controlled

by the heat input (laser) and heat dissipation (by conduction, radiation and convection). The numerical results show that at the same build height, the deposits in the centre of the small-plate (Case S0) and in the corner of the large-plate (Case L1) achieve respectively the highest and lowest average temperatures of 665ºC and 468ºC at the valley of the thermal curves, with a decreasing peak temperature, while another two cases have a similar average temperature of approximately 560ºC. Besides, the small-plate reaches the quasi-steady stage after finishing the 3rd layer, much faster than the large-plate, which reaches it after the deposition of the 12th layer.

3.2. Macrostructures

Figure 6 shows the optical macroscopic cross-sections in the Y-Z plane from the DED blocks. Note that macrostructures are characterized by coarse columnar prior-β grains (0.5 ± 0.2 mm wide) and layer bands (dark grey area). The columns of prior-β grains go through the horizontal bands and the multiple layers. The bands are regularly distributed throughout the metal deposition. Similar results are also observed in specimens made by other AM technologies (Neikter et al. 2018; Qiu et al, 2015). Interestingly, the spacing between the adjacent bands in the centre of samples is about 2 layer-thicknesses (Figures 6(a) and 6(c)), while in the corner of the deposition the spacing is about 4 layer-thicknesses (Figures 6(b) and 6(d)). In the top of each sample, a band-free region of approximately the last 7~8 deposition-layers is observed.

3.3. Microstructures

Figure 7 shows the transformation microstructures across one band framed in yellow in Figures 6(a)-(b), corresponding to the case of the small substrate. Note that the microstructures discerned in the band and the normal region are significantly different. The normal region without band is composed of uniform basketweave

microstructures. Contrariwise, the microstructures in the band area feature colony structures. Similar results have been reported in references (Li et al. 2019).

Figure 8 shows the microstructures at the different deposition positions, arising from the normal area located at the middle between two adjacent bands. Figure 9 compares the average sizes of the α laths, referring to the microstructures displayed in Figure 8. It should be mentioned that only typical basketweave microstructures is accounted for in the statistical results. Overall, the morphology and the scale of the α phase present remarkable differences for the different samples. It can be noted from Figure 8 that at the top, the α basketweave in each specimen is fine. Also, a handful of massive α_m and martensite α′ structures are observed when using the small and large baseplates, respectively. At the half-height and basement of the deposits, the microstructural size reduces in the order of Case S0 > Case S1 > Case L0 > Case L1. Notably, the α-laths in Case S0 (Figure 8(a)) are notoriously coarsened and some coarsened lamellar are broken. In addition, a few massive structures also are found at the bottom of the build on the large baseplate (Figures 8(g) and (j)).

3.4. Microhardness

The mean microhardness measured in different deposition positions is presented in Figure 10. It can be seen that the microhardness values at the top of all cases are almost the same, about 330 HV, relatively higher than those at the lower build height in the case of the small substrate. Obviously, this is attributable to the corresponding microstructure, consisting of fine basketweave and α_m/α′ structures (Figure 8), which usually have extremely high strength, but poor plasticity (Paydas et al. 2015). Notably, Case L1 obtains the highest microhardness in both the bottom and middle positions, due to the finest α lamellar involved (Figure 9). Except for Case L1, the microhardness at the half-height decreases due to the relatively coarser α microstructures, especially for

Case S0. At the basement of the build, the microhardness falls in the order of Case L1 > Case L0 > Case S1 > Case S0, while the reverse order corresponds to the microstructural size. In general, the thicker α microstructure, the lower the strength while the better the damage tolerance (Åkerfeldt et al. 2016; Zhao et al. 2020).

4. Discussion

4.1. Formation of layer bands

The colony microstructure obtained in this work in the layer band region of the DED blocks is similar to that obtained in previous reports about the Ti6Al4V single-walls fabricated by various AM methods (Neikter et al. 2018; Shrestha et al. 2021). Ho et al. 2019 carried out simulations in the dilatometer and found that the formation mechanism of such microstructural bands can be attributed to re-heating to just below T_β (≈1000°C (Baykasoğlu et al. 2020)). However, the formation of layer bands is different in AM single-walls and blocks. In AM single-walls, the separation distance between layer bands corresponds to the average layer-thickness because the temperature distribution in the building of each layer is similar due to the use of simplex adding path. In this work it is found that in AM blocks the complexity of the thermal history dramatically increases when utilizing the interwoven building strategy, resulting in completely different band distributions in the centre and corner of the builds as shown in Figure 6.

In order to figure out the mechanism for the formation of such band distributions, Figure 11 displays the extension of the molten pool and the region corresponding to the temperature range of 900~1000°C ($TR_{\Delta 100}$) beneath the molten pool during the whole of the DED process. Data shown is for the small substrate simulation, but very similar phenomena occur for the large substrate.

Figure 11(a) shows the evolution of the $TR_{\Delta 100}$ position when the molten pool traverses the centre of the build. It is observed that when even layers are deposited at the centre of the baseplate, the top of $TR_{\Delta 100}$ is approximately two layer-heights lower than that when depositing the previous odd layer. The reason for such fall of $TR_{\Delta 100}$ is that the heat is significantly accumulated at the depositing centre when the shorter scanning vector is used to fabricate even layers, as shown in Figures 12(a)-(d), contributing to deepen the molten pool. The β-transus thus shifts downward responding to the deepening of the molten pool. The resultant decline of $TR_{\Delta 100}$ during the deposition of even layers (i.e. the 22^{nd} layer) causes a full β annealing in the upper region of the α+β phase field generated in the deposition of the previous odd (21^{st}) layer. Also, the region corresponding to the top of $TR_{\Delta 100}$ is re-heated to just below T_β, which results in the layer band featured by colony structures. In subsequent thermal cycling, such colony structure is retained because the temperature in this band layer fails to approach T_β. Hence, as the number of layers and the height of the block increase, the layer band in the centre of the block is generated in the deposition of the even layers only, explaining why the spacing of the bands observed in Figure 6(a) is approximately 2 layer-thick.

Figure 11(b) gives the $TR_{\Delta 100}$ evolution as the molten pool passes the corner of the block printed on the small baseplate. Interestingly, when looking at the deposition of 4 consecutive layers (i.e. the 7^{th}~10^{th} layers), the upper limit of $TR_{\Delta 100}$ gradually goes down with respect to the top of the build. This is associated with the printing sequence used (Figure 2). Taking the temperature field evolution of the 19^{th}~22^{nd} layers as an example, as shown in Figures 12(e-h), it can be seen that not only the 20^{th} and 21^{st} layers end but also the 22^{nd} layer starts at the corner, contributing to the local heat accumulation. Thus, the molten pool gradually deepens and the resulting $TR_{\Delta 100}$ drops down along the building direction. Noticeably, the region above $TR_{\Delta 100}$ is fully β-

annealed in the deposition of the 22nd layer, while the top of $TR_{\Delta 100}$ is re-heated to just below T_β, leading to the formation of the layer band. One formed, this band remains in the following thermal cycling. Similarly, during the depositing of the next four layers, the bands produced during the printing of the 23rd~25th layers fail to survive because they suffer a full β annealing before or during depositing the 26th layer, and only the layer band formed while fabricating the 26th layer can survive. Similar processes repeat every 4-layers. Hence, the corner bands are evenly spaced through the deposit, 4 layer-heights apart (Figures 6(b) and (d)).

Figure 11 also compares the predicted and experimental locations of the layer bands. Observe that on the whole, the model presents a high prediction precision, allowing for experimental error.

4.2. Relation between the microstructures and thermal history

The microstructural features of the metal deposition are closely related to the thermal history experienced during the DED process. In order to elucidate the development of the α morphology in Figure 8, the temperature curves predicted in Figure 5 are further analysed.

Figure 13 displays the evolution of the temperature and the cooling rate at the top of the blocks in the DED process. Note that when the material is just added, an extremely high cooling rate (above 410°C/s) occurs at the vicinity of the molten pool, favouring the martensitic transformation. However, the full β annealing in subsequent thermal cycling results in a complete dissolution of all kinds of α phases previously formed (Wang et al. 2019). Hence, only when the peak temperature is below T_β, the microstructure originally formed can be completely or partially retained. For the top of the build, there are almost no re-heating and cooling cycles after the last cooling from the temperature above T_β. Therefore, it can be deduced that the cooling rates in the last

cooling from T_β to T_{diss} (747°C (Wang et al. 2019)), marked in grey, should have a significant influence on the microstructure of the deposit. It can be seen from Figure 13 that the cooling rapidly declines and stabilizes at a low level (below 20°C/s) in such cooling stage. When temperature reaches the martensite-start temperature (M_s=851°C), the corresponding cooling rates, marked in green, are lower than 20°C/s except for Case L1 (33°C/s), failing to explain the existence of the α_m and α′ structures observed at the top of the build (see Figure 8). As mentioned before, the DED process features localized forced convection resulting from the feeding nozzles, which causes a higher cooling rate for the top layer (Heigel, Michaleris, and Palmer 2016). However, this is not considered in the thermal model adopted. Hence, the local cooling rate is underestimated in the simulation. In addition to α_m/α′, fine basketweave microstructures are also observed at the top of the build (Figure 8). Obviously, they are attributable to such slow cooling stage. Noticeably, Case S0 undergoes the longest cooling time (from T_β to T_{diss}) under the lowest cooling rate and thus produces coarser α-laths compared with other cases (Figure 9).

Unlike the top region, the lower deposits go through several heating and cooling cycles after the peak temperature is smaller than T_β, while the corresponding cooling rates in these cycles are lower. As a result, the original basketweave microstructures coarsen and the potential α_m/α′ structures initially formed are dissolved in varying degrees, significantly different from the mixed microstructures composed of fine α lamellar and much of α_m/α′ structures at the top of the build (Figure 8).

The coarsening of α basketweave observed in the lower deposition positions can be explained by two possible mechanisms. The first mechanism is conventional Ostwald ripening, which is a diffusion-controlled process driven by reducing the interfacial energy; i.e., small crystal structures dissolve and redeposit onto larger ones under

constant or varying temperature over time (Zhu et al. 2018). The second mechanism is based on multi dissolution and precipitation transformations, as proposed by Ho et al. 2019 and illustrated in Figure 15. It can be seen from Figure 14(a1) that upon cooling from above T_β to below T_{diss}, fine basketweave structures are produced at the basement of the build. During the printing of the 13^{th}~38^{th} layers, the bottom microstructures suffer several thermal cycles under small cooling and heating rates (below 20°C/s). In heating, an interface-controlled re-growth of β phase occurs while all α laths with different sizes shrink. Notably, the thinnest α lamellar vanishes and only a few bigger ones survive in such heating (Figure 14(a2)). Once temperature falls, the surviving α lamellas grow back through consumption of the β matrix. As a result, the dimension of α plates increases due to the reduction in the lamellar number (Figure 14(a3)). After heating and cooling several times between T_β and T_{diss}, the lamellar α is coarsened and saved after finishing the 38^{th} layer, allowing for no further phase transformation in the fabrication of the last two layers. Also, some longer prior-α laths are broken (see Figures 8(a)-(b)) during coarsening. It should be mentioned that the transformation coarsening mechanism, from migration of the α/β interfaces between T_β and T_{diss}, is much faster than the interfacial energy-driven Ostwald ripening.

Until now, several classic theories like MLSW model have been developed to quantify the growth (coarsening) of the second phase during the isothermal processes (Semiatin et al. 2019; Zhang et al. 2021). However, coarsening observed in AM parts is obtained under repeated heating and cooling cycles, which is different from the constant temperature assumption in MLSW theory. So far, no theoretical model can directly quantify Ostwald ripening or transformation coarsening mechanism at variable temperature. However, Ostwald ripening theory has illustrated that the particle coarsening depends on two factors in terms of the coarsening time and the diffusion

coefficient (Vengrenovitch 1982). Noticeably, the diffusion coefficient is positively related to temperature. The higher the temperature or the longer the time, the greater the diffusion coefficient. Therefore, the coarsening level can be determined by time and temperature involved. Based on this, the integral area (IA), i.e., the area under the evolving curve of temperature versus time, is proposed to assess the coarsening level, as it considers the combined effect of both time and temperature. It should be noted that the larger is the IA, the longer is the acting time and/or the higher is the sustained temperature, favouring the coarsening of α plates. As known, diffusion-controlled Oswald ripening can happen in a wide range of temperatures. Thereby, starting when the peak temperature is smaller than T_β, the integral area (IA_{Osw}) below the thermal curve, coloured in yellow in Figure 14(b), is calculated and plotted in Figure 15(a). Observe that the IA_{Osw} values at the same build-height are close for four cases, whereas the microstructural characteristics in Figure 8 are markedly different. This illustrates that Ostwald ripening hardly explains the coarsening of the α lamellar observed in these cases.

Differently, coarsening by multi dissolution and precipitation transformations is just related with the α/β interface migration between T_β and T_{diss} during repeated thermal cycles. Thus, the representative integral area (IA_{trans}) is coloured in grey in Figure 14(a), and the corresponding value for each case is plotted in Figure 15(b). Note that Case S0 obtains the highest IA_{trans}, corresponding to the coarsest α-laths (Figure 8) and the lowest microhardness (Figure 10). In contrast, in Case L1 a slight coarsening of basketweave α structure appears (see Figures 8(j)-(k)), being subjected to the smallest IA_{trans}. For Case S1 and Case L0, the coarsening level is moderate and in line with the corresponding IA_{trans}. Therefore, the coarsening behaviour in these cases is primarily driven by transformation mechanism, rather than by Oswald ripening.

4.3 Thermal-microstructure-microhardness relationship

Figure 16 shows the relationship between the thermal history, the microstructure and the microhardness. During thermal cycling, the difference in size of α lamellar depends on the subsequent coarsening and this can be assessed by the IA_{trans} index. Quantitatively, the width of α lamellar is approximately a linear function of IA_{trans}, as shown in Figure 16(a). Based on this, the size of α lamellar can be predicted from the thermal history. Furthermore, a fitted relation between the microhardness and the width of α lamellar is presented in Figure 16(b), similarly to the Hall-Petch relation (Hansen 2004). It should be mentioned that the microhardness results obtained from the samples do not take into account the massive or martensite structures. Obviously, the hardness decreases as the α-laths coarsen. The reason for this is that increasing α size decreases the amount of sub-structure boundaries. The stresses necessary to move dislocations across such boundaries rise as material deforms, accounting for the reduction in the microhardness.

The thermal-microstructure-microhardness relationship helps understand their inner connection and the role of the thermal history, as the bridge between AM variables and microstructure. Also, it provides guidance to designing the microstructure of AM titanium alloy via optimizing the thermal history.

5. Conclusions

This work studies the relationship between key microstructural characteristics, microhardness and thermal histories involved in Ti6Al4V DED processes. A FE thermal model for DED is firstly calibrated by in-situ measurement involving two part-scale blocks deposited on two differently dimensioned baseplates. This done, the predicted temperature data is used to study the formation of layer bands and to explain

how the choice of AM parameters affects the metallurgical evolution. The main conclusions drawn are as follow:

(1) Comparison between the computed results and in-situ measured evidence presents a remarkable agreement. Using the calibrated model, the full-field temperature is accurately predicted to quantitatively analyse the thermal-microstructure relation in the DED process.

(2) The substrate size significantly affects local heat accumulation and the entire thermal history in the building process. As a result, the final microstructural characteristics at different deposition positions of the blocks differ from each other. Based on this, substrate can be designed to control the thermal-metallurgical evolution.

(3) The layer bands are evenly spaced through the deposits, 2 and 4 layer-thick apart in the centre and corner of two part-scale blocks, respectively. Such distributions are due to the different evolutions of the relevant temperature range just underneath T_β controlled by the building sequence used.

(4) The final microstructure at the top of the build is closely linked to the cooling rates in the last cooling from T_β to T_{diss}. However, this is not the case for the lower part of the deposited blocks since repeated thermal cycles suffered yield a pronounced microstructural change.

(5) The coarsening of α-laths in the normal region is associated with the integral area IA_{trans} as temperature of the thermal cycles varies between T_β and T_{diss}. Such coarsening is primarily driven by the transformation mechanism featured by the migration of the α/β interface, rather than that of conventional Ostwald ripening.

(6) The proposed IA_{trans} can be used to establish a quantitative thermal-microstructural relationship for Ti6Al4V and to link AM variables with metallurgy. By designing the fabricating process, it is possible to optimize the microstructure distribution to improve the overall quality of AM parts.

Declaration of Competing Interest

None.

Acknowledgement

This work was funded by the National Key Technologies R & D Program (No. 2016YFB1100100), the National Natural Science Foundation of China (Grants No. 51874245), the European KYKLOS 4.0 project (No. 872570), the Severo Ochoa Programme for Centres of Excellence in R&D (CEX2018-000797-S) and the China Scholarship Council (No. 201906290011).

References

Åkerfeldt, P., M. Antti, and R. Pederson. 2016. "Influence of microstructure on mechanical properties of laser metal wire-deposited Ti-6Al-4V." Materials Science and Engineering: A 674: 428-437.

Baiges, J., M. Chiumenti, C. A. Moreira, M. Cervera, and R. Codina. 2021. "An Adaptive Finite Element strategy for the numerical simulation of Additive Manufacturing processes." Additive Manufacturing 37: 101650.

Baykasoğlu, C., O. Akyildiz, M. Tunay, and A. C. To. 2020. "A process-microstructure finite element simulation framework for predicting phase transformations and microhardness for directed energy deposition of Ti6Al4V." Additive Manufacturing 35: 101252.

Cervera, M., C. A. Saracibar, and M. Chiumenti. 2002. "Comet: Coupled mechanical and thermal analysis. data input manual." Barcelona: International Center for Numerical Methods in Engineering (CIMNE).

Chiumenti, M., E. Neiva, E. Salsi, M. Cervera, S. Badia, J. Moya, Z. Chen, C. Lee, and C. Davies. 2017. "Numerical modelling and experimental validation in Selective Laser Melting." Additive Manufacturing 18: 171-185.

Chiumenti, M., M. Cervera, A. Salmi, C. A. Saracibar, N. Dialami, and K. Matsui. 2010. "Finite element modeling of multi-pass welding and shaped metal deposition processes." Computer methods in applied mechanics and engineering 199(37-40): 2343-2359.

Chiumenti, M., M. Cervera, N. Dialami, B. Wu, L. Jinwei, and C. A. Saracibar. 2016. "Numerical modeling of the electron beam welding and its experimental validation." Finite Elements in Analysis and Design 121: 118-133.

Chiumenti, M., X. Lin, M. Cervera, W. Lei, Y. Zheng, and W. Huang. 2017. "Numerical simulation and experimental calibration of Additive Manufacturing by blown powder technology. Part I: thermal analysis." Rapid Prototyping Journal 23(2): 448-463.

Crespo, A., and R. Vilar. 2010. "Finite element analysis of the rapid manufacturing of Ti–6Al–4V parts by laser powder deposition." Scripta Materialia 63(1): 140-143.

Fan, W., H. Tan, X. Lin, and W. Huang. 2018. "Microstructure formation of Ti-6Al-4 V in synchronous induction assisted laser deposition." Materials & Design 160: 1096-1105.

García, D., L. E. García, and I. Gómez. 2010. "An interface between an hp-adaptive finite element package and the pre-and post-processor GiD." Finite elements in analysis and design 46(4): 328-338.

Goh, G., S. Sing, and W. Yeong. 2021. "A review on machine learning in 3D printing: Applications, potential, and challenges." Artificial Intelligence Review 54(1): 63-94.

Hansen, N. 2004. "Hall–Petch relation and boundary strengthening." Scripta materialia 51(8): 801-806.

Heigel, J. C., P. Michaleris, and T. A. Palmer. 2016. "Measurement of forced surface convection in directed energy deposition additive manufacturing." Proceedings of the Institution of Mechanical Engineers, Part B: Journal of Engineering Manufacture 230(7): 1295-1308.

Ho, A., H. Zhao, J. W. Fellowes, F. Martina, A. E. Davis, and P. B. Prangnell. 2019. "On the origin of microstructural banding in Ti-6Al4V wire-arc based high deposition rate additive

manufacturing." Acta Materialia 166: 306-323.
Kelly, S. M., and S. L. Kampe. 2004. "Microstructural evolution in laser-deposited multilayer Ti-6Al-4V builds: Part II. Thermal modeling." Metallurgical and Materials Transactions A 35(6): 1869-1879.
Kobryn, P. A., and S. L. Semiatin. 2003. "Microstructure and texture evolution during solidification processing of Ti–6Al–4V." Journal of Materials Processing Technology 135(2-3): 330-339.
Kuo, C., C. Chua, P. Peng, Y. Chen, S. Sing, S. Huang, and Y. Su. 2020. "Microstructure evolution and mechanical property response via 3D printing parameter development of Al–Sc alloy." Virtual and Physical Prototyping 15(1): 120-129.
Kürnsteiner, P., M. B. Wilms, A. Weisheit, B. Gault, E. A. Jägle, and D. Raabe. 2020. "High-strength Damascus steel by additive manufacturing." Nature 582(7831): 515-519.
Liu, Z., B. He, T. Lyu, and Y. Zou. 2021. "A Review on Additive manufacturing of titanium alloys for aerospace applications: directed energy deposition and beyond Ti-6Al-4V." JOM 1-15.
Liu, Z., C. Chua, K. Leong, K. Kempen, L. Thijs, E. Yasa, J. Van-Humbeeck, and J. Kruth. 2011. "A preliminary investigation on selective laser melting of M2 high speed steel." In 5th International Conference on Advanced Research and Rapid Prototyping, Leiria, Portugal, 339-346.
Li, J., X. Lin, P. Guo, and W. Huang. 2019. "Effect of layer band and heterogeneity of microstructure on electrochemical dissolution of laser solid formed Ti-6Al-4V alloy." Journal of Laser Applications 31(2): 022312.
Li, Y., K. Zhou, P. Tan, S. Tor, C. Chua, and K. Leong. 2018. "Modeling temperature and residual stress fields in selective laser melting." International Journal of Mechanical Sciences 136: 24-35.
Li, Y., K. Zhou, S. Tor, C. Chua, and K. Leong. 2017. "Heat transfer and phase transition in the selective laser melting process." International Journal of Heat and Mass Transfer 108: 2408-2416.
Lu, X., M. Chiumenti, M. Cervera, J. Li, X. Lin, L. Ma, G. Zhang, and E. Liang. 2021. "Substrate design to minimize residual stresses in Directed Energy Deposition AM processes." Materials & Design 202: 109525.
Lu, X., X. Lin, M. Chiumenti, M. Cervera, Y. Hu, X. Ji, L. Ma, and W. Huang. 2019. "In situ measurements and thermo-mechanical simulation of Ti–6Al–4V laser solid forming processes." International Journal of Mechanical Sciences 153: 119-130.
Lu, X., X. Lin, M. Chiumenti, M. Cervera, Y. Hu, X. Ji, L. Ma, H. Yang, and W. Huang. 2019. "Residual stress and distortion of rectangular and S-shaped Ti-6Al-4V parts by Directed Energy Deposition: Modelling and experimental calibration." Additive Manufacturing 26: 166-179.
Lu, X., X. Lin, M. Chiumenti, M. Cervera, J. Li, L. Ma, L. Wei, Y. Hu, and W. Huang. 2018. "Finite element analysis and experimental validation of the thermomechanical behavior in laser solid forming of Ti-6Al-4V." Additive Manufacturing 21: 30-40.
Neikter, M., P. Åkerfeldt, R. Pederson, M-L. Antti, and V. Sandell. 2018. "Microstructural characterization and comparison of Ti-6Al-4V manufactured with different additive manufacturing processes." Materials Characterization 143: 68-75.
Paydas, H., A. Mertens, R. Carrus, J. Lecomte-Beckers, and J. T. Tchuindjang. 2015. "Laser cladding as repair technology for Ti–6Al–4V alloy: Influence of building strategy on microstructure and hardness." Materials & Design 85: 497-510.
Qian, L., J. Mei, J. Liang, and X. Wu. 2005. "Influence of position and laser power on thermal history and microstructure of direct laser fabricated Ti–6Al–4V samples." Materials science and technology 21(5): 597-605.
Qiu, C., G. A. Ravi, C. Dance, A. Ranson, S. Dilworth, and M. M. Attallah. 2015. "Fabrication of large Ti–6Al–4V structures by direct laser deposition." Journal of Alloys and Compounds 629: 351-361.
Ren, Y. M., X. Lin, X. Fu, H. Tan, J. Chen, and W. D. Huang. 2017. "Microstructure and deformation behavior of Ti-6Al-4V alloy by high-power laser solid forming." Acta

Materialia 132: 82-95.
Sandgren, H. R., Y. Zhai, D. A. Lados, P. A. Shade, J. C. Schuren, M. A. Groeber, P. Kenesei, and A. G. Gavras. 2016. "Characterization of fatigue crack growth behavior in LENS fabricated Ti-6Al-4V using high-energy synchrotron x-ray microtomography." Additive Manufacturing 12: 132-141.
Semiatin, S. L., N. C. Levkulich, A. R. C. Gerlt, E. J. Payton, J. S. Tiley, F. Zhang, R. A. MacKay, R. V. Miner, and T. P. Gabb. 2019. "High-Temperature Static Coarsening of Gamma-Prime Precipitates in NiAlCr-X Single Crystals." Metallurgical and Materials Transactions A 50(5): 2289-2301.
Shrestha, S., R. P. Panakarajupally, M. Kannan, G. Morscher, A. L. Gyekenyesi, and O. E. Scott-Emuakpor. 2021. "Analysis of microstructure and mechanical properties of additive repaired Ti–6Al–4V by Direct Energy Deposition." Materials Science and Engineering: A 806: 140604.
Tan, J., S. Sing, and W. Yeong. 2020. "Microstructure modelling for metallic additive manufacturing: a review." Virtual and Physical Prototyping 15(1): 87-105.
Tan, P., F. Shen, B. Li, and K. Zhou. 2019. "A thermo-metallurgical-mechanical model for selective laser melting of Ti6Al4V." Materials & Design 168: 107642.
Tang, Z., W. Liu, Y. Wang, K. Saleheen, Z. Liu, S. Peng, Z. Zhang, and H. Zhang. 2020. "A review on in situ monitoring technology for directed energy deposition of metals." The International Journal of Advanced Manufacturing Technology 1-27.
Vengrenovitch, R. D. 1982. "On the Ostwald ripening theory." Acta metallurgica 30(6): 1079-1086.
Wang, J., X. Lin, J. Li, Y. Hu, Y. Zhou, C. Wang, Q. Li, and W. Huang. 2019. "Effects of deposition strategies on macro/microstructure and mechanical properties of wire and arc additive manufactured Ti6Al4V." Materials Science and Engineering: A 754: 735-749.
Wolff, S. J., S. Lin, E. J. Faierson, W. K. Liu, G. J. Wagner, and J. Cao. 2017. "A framework to link localized cooling and properties of directed energy deposition (DED)-processed Ti-6Al-4V." Acta Materialia 132: 106-117.
Zhang, G., J. Chen, M. Zheng, Z. Yan, X. Lu, X. Lin, and W. Huang. 2020. "Element vaporization of Ti-6AL-4V alloy during selective laser melting." Metals 10(4): 435.
Zhang, J., L. Liu, T. Huang, J. Chen, K. Cao, X. Liu, J. Zhang, and H. Fu. 2021. "Coarsening kinetics of γ′ precipitates in a Re-containing Ni-based single crystal superalloy during long-term aging." Journal of Materials Science & Technology 62: 1-10.
Zhang, J., Y. Liu, M. Bayat, Q. Tan, Y. Yin, Z. Fan, S. Liu, J. H. Hattel, M. Dargusch, and M. Zhang. 2021. "Achieving high ductility in a selectively laser melted commercial pure-titanium via in-situ grain refinement." Scripta Materialia 191: 155-160.
Zhang, Y., C. Lim, C. Tang, and B. Li. 2021. "Numerical investigation on heat transfer of melt pool and clad generation in directed energy deposition of stainless steel." International Journal of Thermal Sciences 165: 106954.
Zhao, Z., J. Chen, H. Tan, J. Tang, and X. Lin. 2020. "In situ tailoring microstructure in laser solid formed titanium alloy for superior fatigue crack growth resistance." Scripta Materialia 174: 53-57.
Zhao, Z., J. Chen, X. Lu, H. Tan, X. Lin, and W. Huang. 2017. "Formation mechanism of the α variant and its influence on the tensile properties of laser solid formed Ti-6Al-4V titanium alloy." Materials Science and Engineering: A 691: 16-24.
Zhu, Y., B. Chen, H. Tang, X. Cheng, H. Wang, and L. Jia. 2018. "Influence of heat treatments on microstructure and mechanical properties of laser additive manufacturing Ti-5Al-2Sn-2Zr-4Mo-4Cr titanium alloy." Transactions of Nonferrous Metals Society of China 28(1): 36-46.

Table 1. Process parameters used for fabricating the blocks by DED.

Laser power P (kW)	Scan speed V (mm/s)	Up-lift height ΔZ (mm)	Feeding rate f (g/min)	Beam diameter d (mm)
2	15.0	0.5	10.0	5.0

Table 2. Temperature-dependent material properties of Ti6Al4V alloy (Lu et al. 2019).

Temperature (°C)	20	205	500	995	1100	1200	1600	1650	2000
Density (kg/m^3)	4420	4395	4350	4282	4267	4252	4198	3886	3818
Thermal conductivity (W/(m·°C))	7.0	8.75	12.6	22.7	19.3	21.0	25.8	83.5	83.5
Heat capacity (J/(kg·°C))	546	584	651	753	641	660	732	831	831

Table 3. The average error of the thermal evolution. (n: total time increments; i: current time increment; x_{exp}: measured temperature; x_{sim}: simulated temperature.)

Error	CH1	CH2	CH3	CH4	CH5	CH6
$\frac{100}{n}\sum_{i=1}^{n}\left\|\frac{(x_{exp})_i-(x_{sim})_i}{(x_{exp})_i}\right\|$	0.37	1.97	2.77	1.47	2.10	0.70

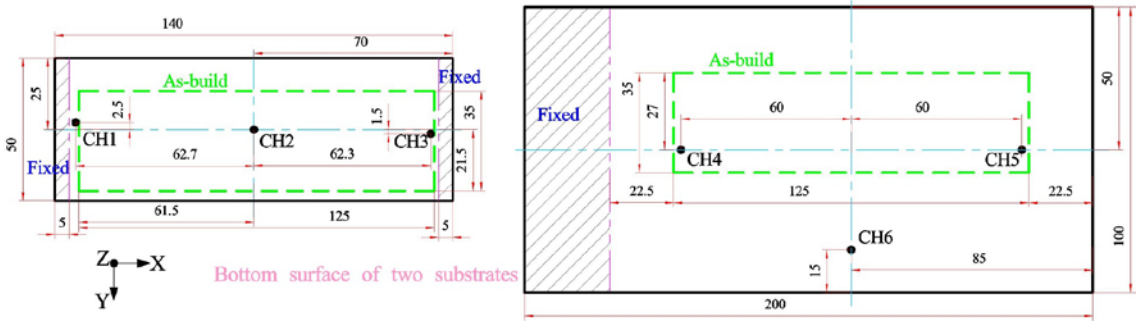

Figure 1. Part dimensions in millimeter and the locations of the thermocouples used to record the thermal history in DED process.

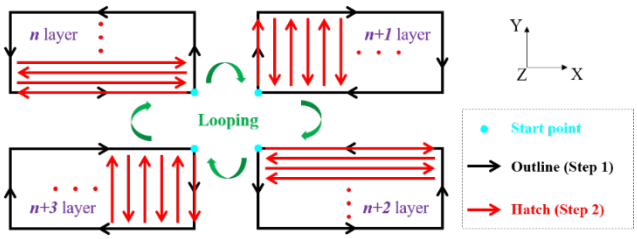

Figure 2. Schematic of the scanning strategy used to build the two blocks.

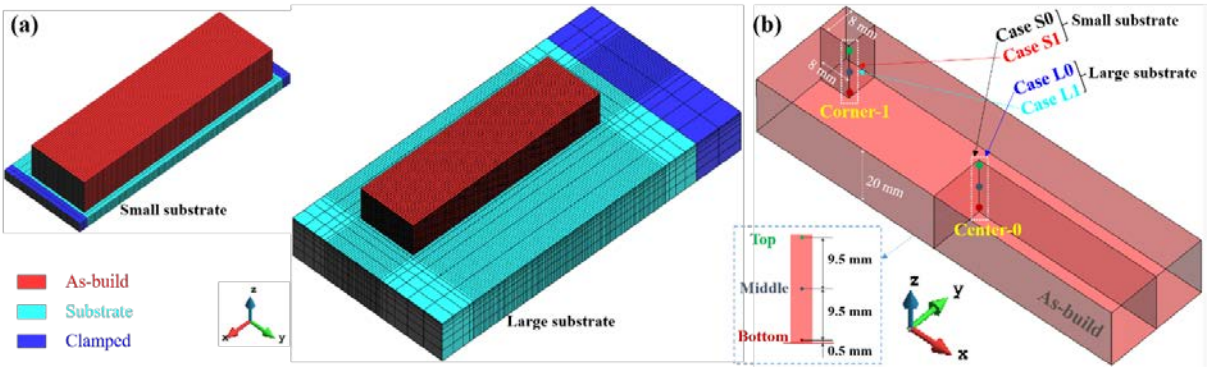

Figure 3. (a) FE mesh model of the blocks deposited on the substrates with different sizes; (b) Schematic of the locations used to extract the predicted thermal history and the microstructures experimentally analysed.

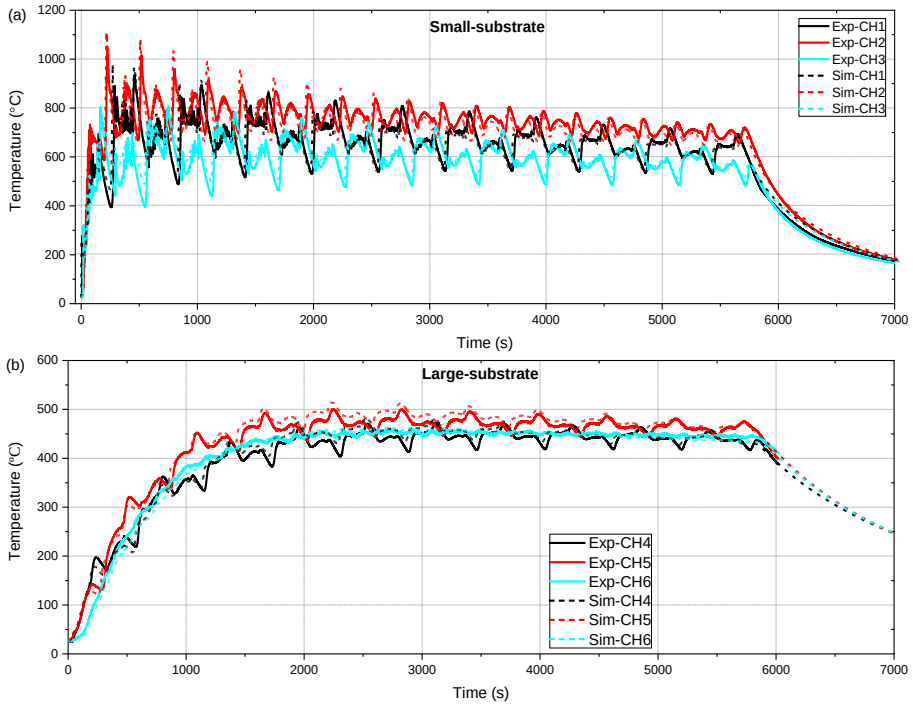

Figure 4. Comparison between the computed and experimental temperature histories: (a) small substrate; (b) large substrate.

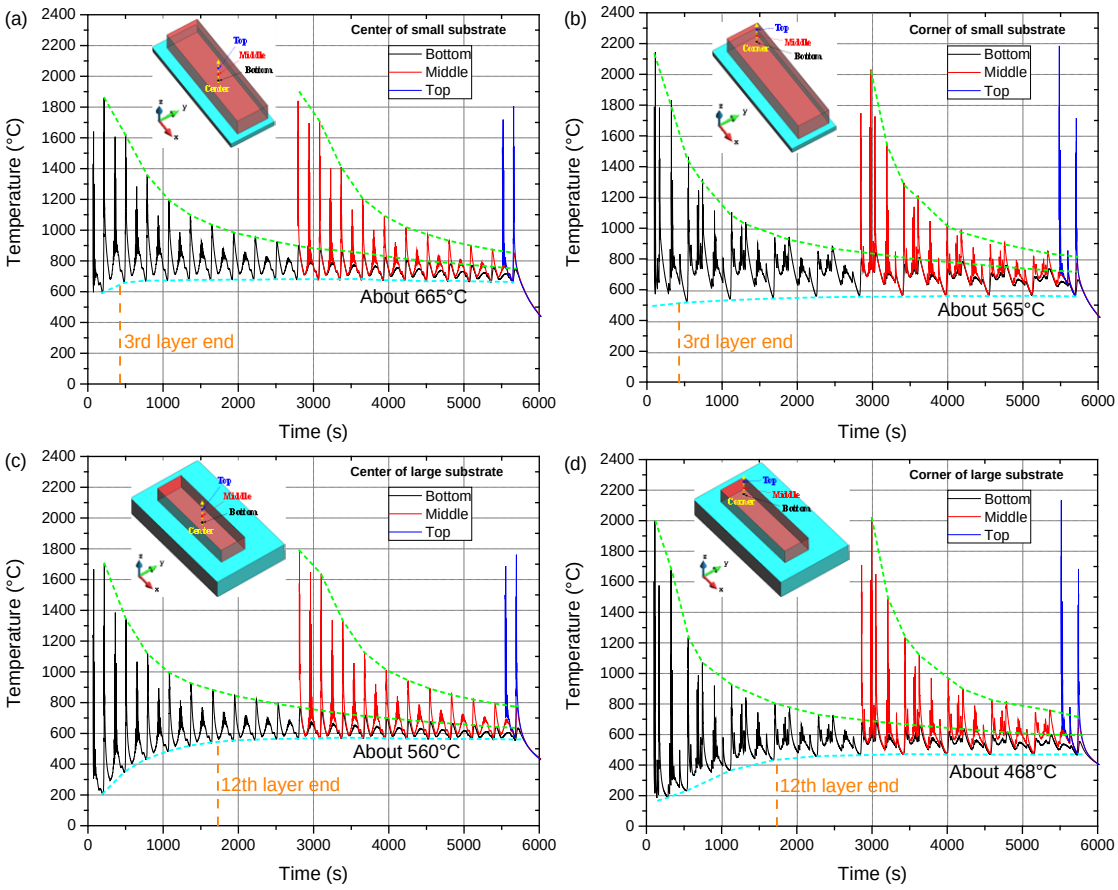

Figure 5. Temperature evolutions in different deposition heights:
(a) Case S0; (b) Case S1; (c) Case L0; (d) Case L1.

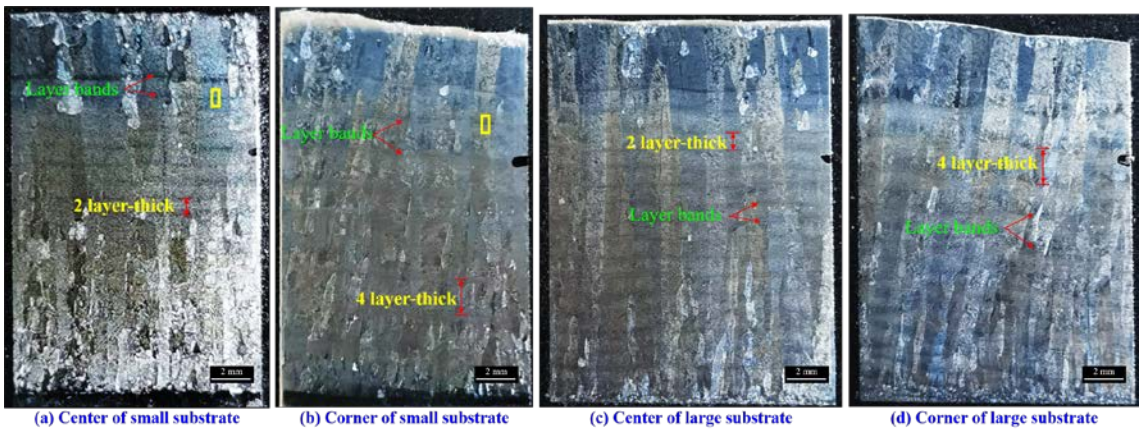

Figure 6. Macroscopic images of the deposited blocks after etching:
(a) Case S0; (b) Case S1; (c) Case L0; (d) Case L1.

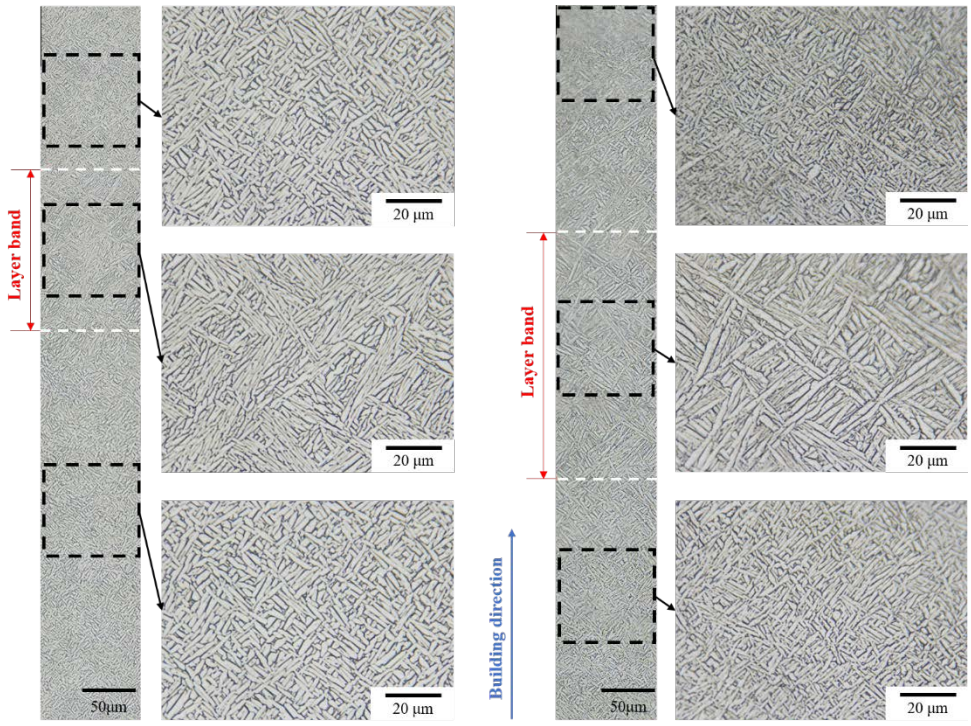

Figure 7. Transformation microstructures across one band framed in yellow in Figures 6(a)-(b).

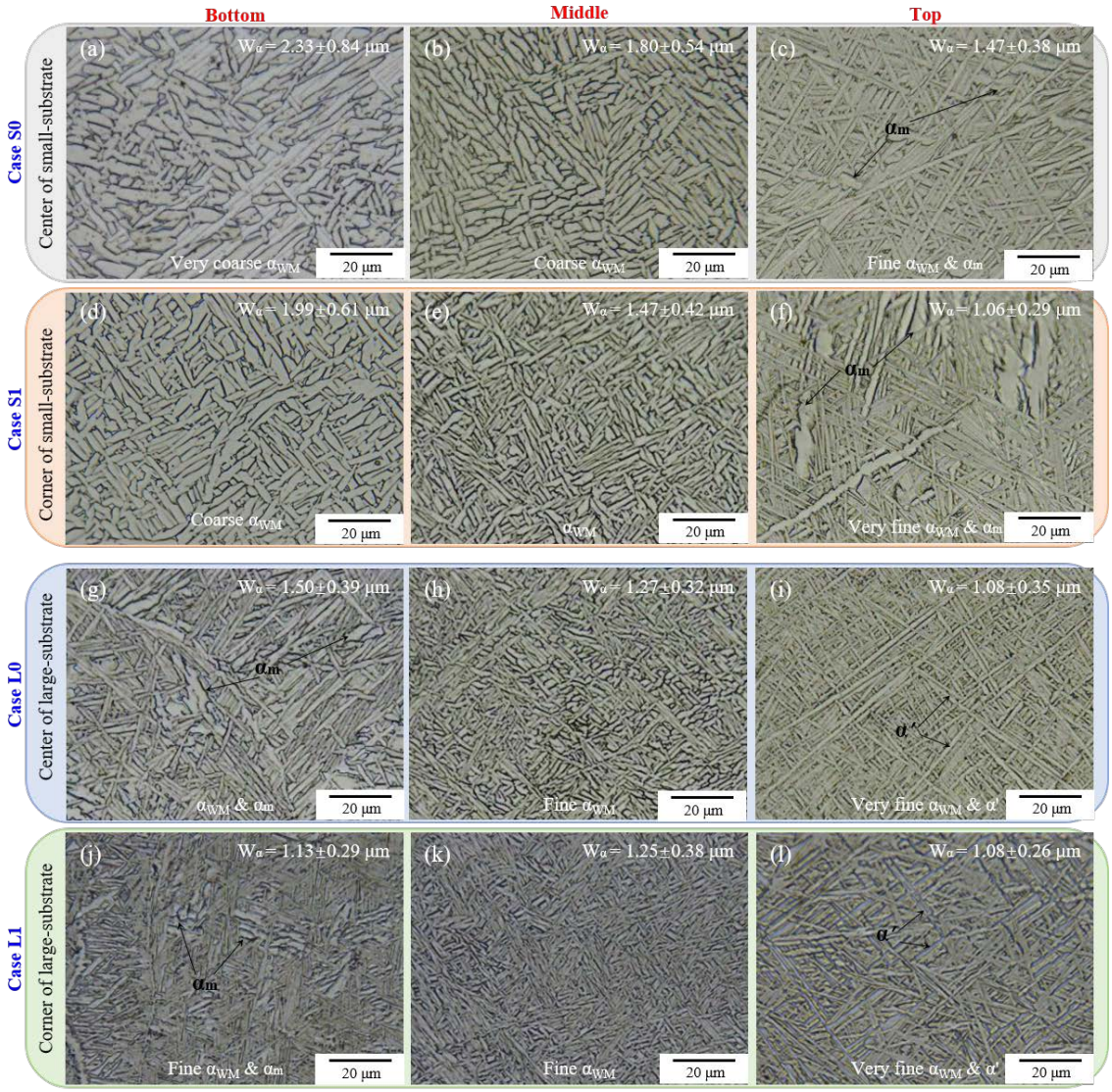

Figure 8. Microstructures observed at different deposition positions.
(α_{BM}: basketweave microstructure; α': martensite; α_m: massive; W_α: average width of α lamellar)

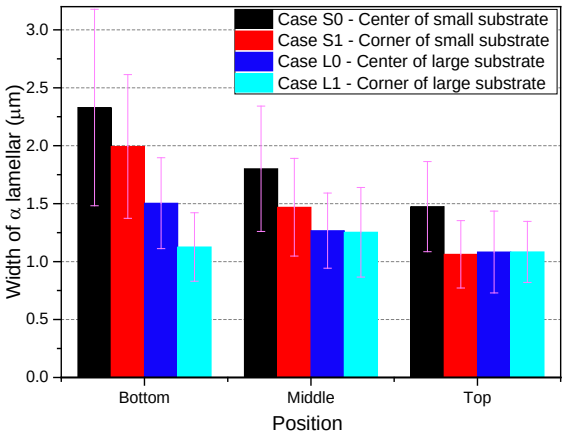

Figure 9. Sizes of the α-lath microstructure for all samples.

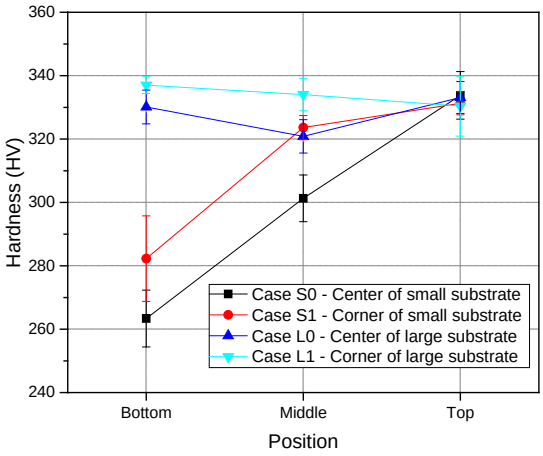

Figure 10. The microhardness in different deposition positions of the DED blocks.

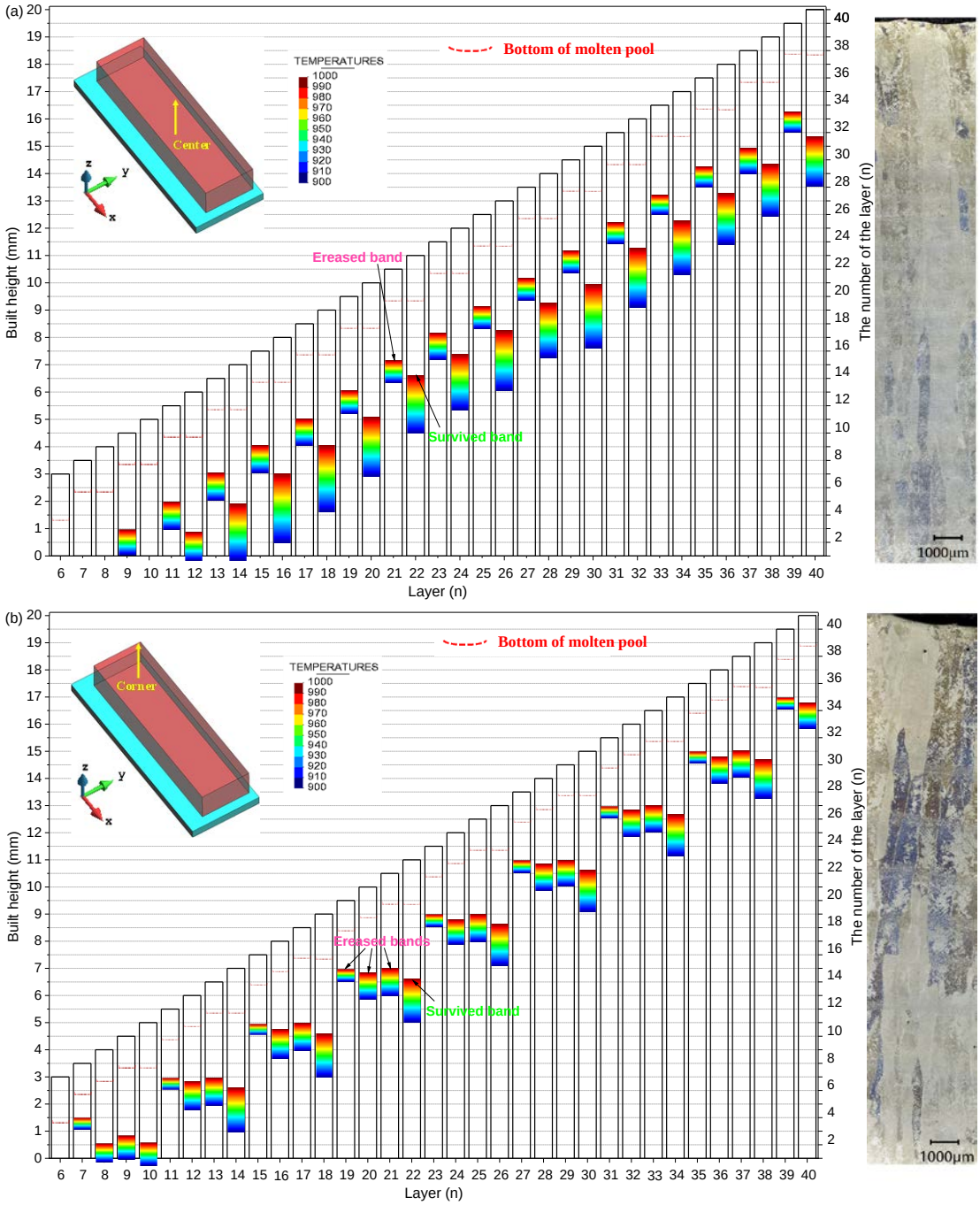

Figure 11. Small substrate: the distributions of the temperature range of 900~1000°C ($TR_{\Delta 100}$) beneath the molten pool in the DED process: (a) Case S0; (b) Case S1.

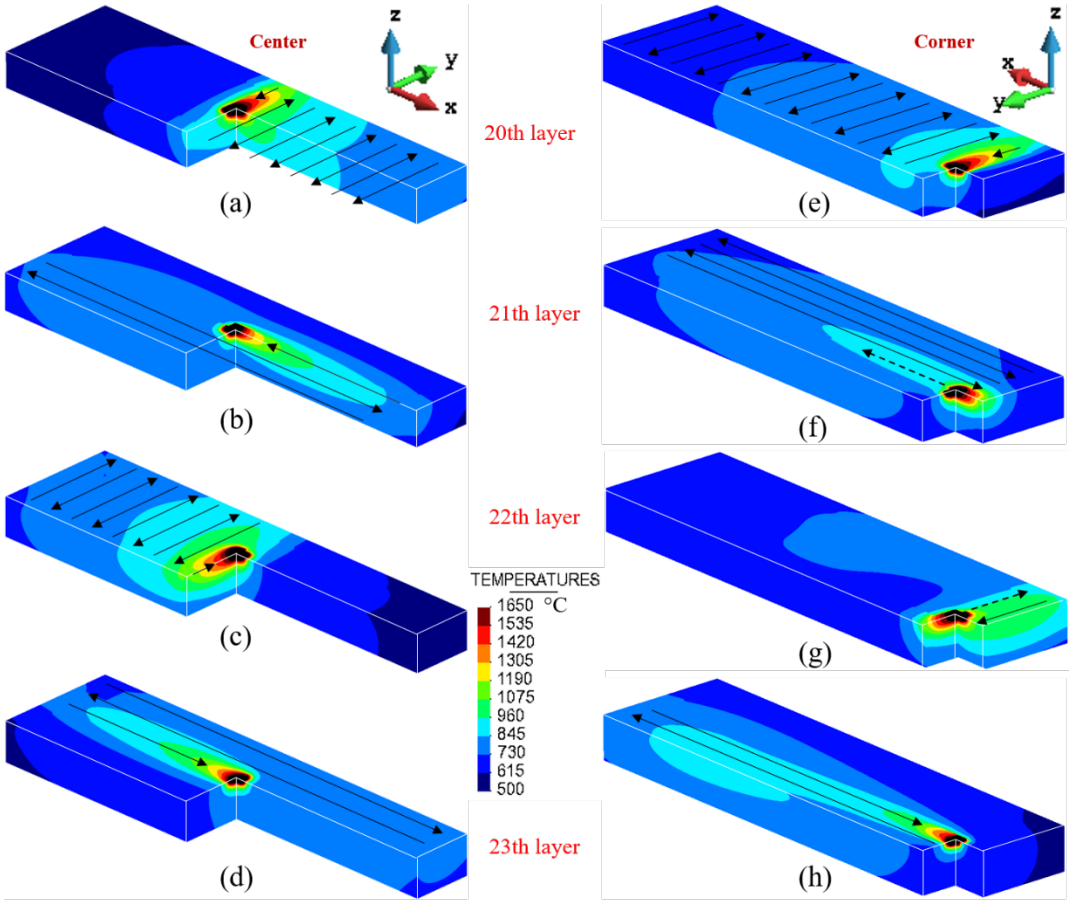

Figure 12. Small substrate: temperature fields when the molten pool reaches (a-d) the centre and (e-h) the corner of the deposit during the fabricating of the 20th~23rd layers. Substrate and partial deposit are hidden for clarity.

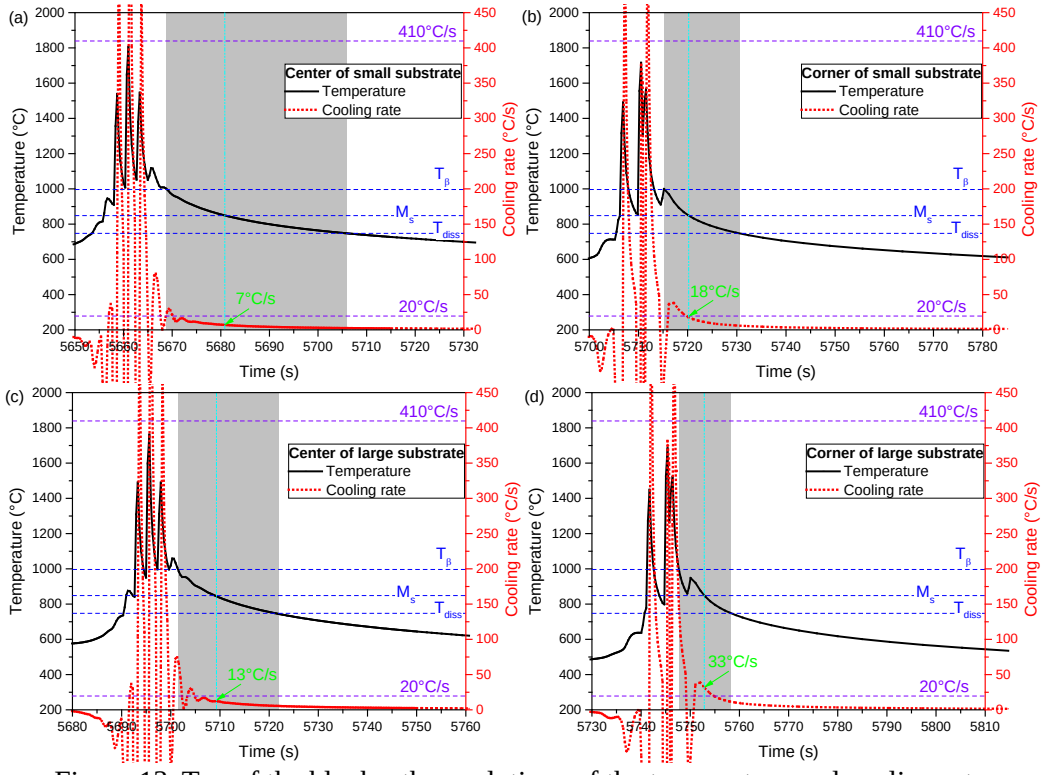

Figure 13. Top of the blocks: the evolutions of the temperature and cooling rate:

(a) Case S0; (b) Case S1; (c) Case L0; (d) Case L1.
(M_s=851°C is martensite-start temperature; >410°C/s is α´ and 20~410°C/s is α´/α_m+α [42]).

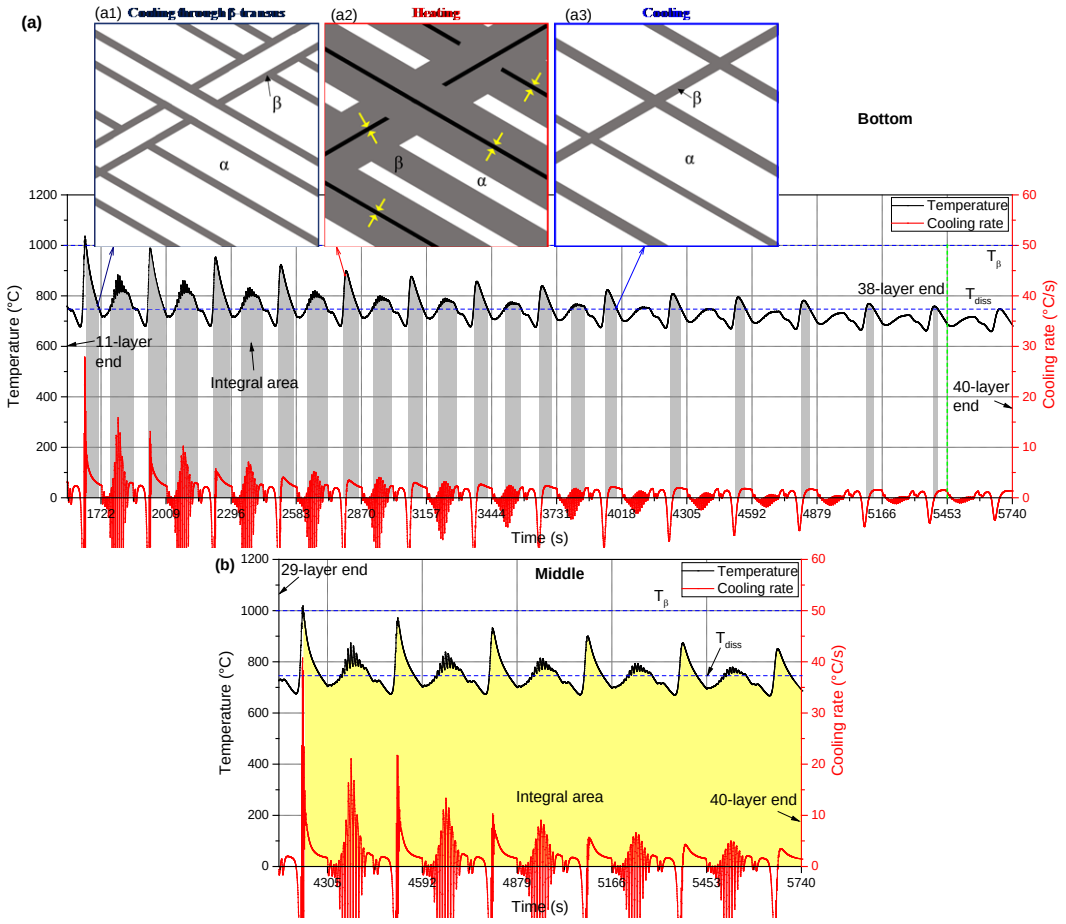

Figure 14. Case S0: Combination of the microstructural evolution and the thermal history: (a) bottom part; (b) middle part.

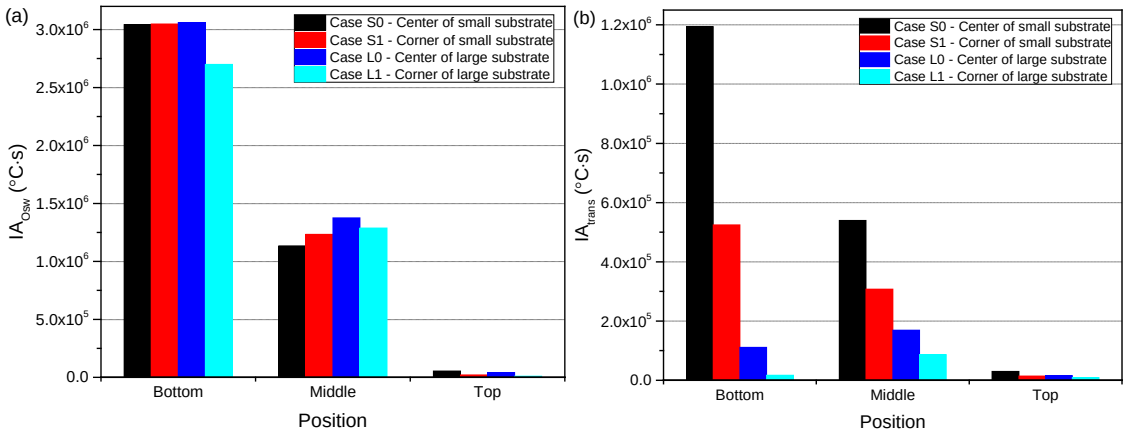

Figure 15. Quantitative index used to assess the coarsening of α-laths: (a) IA_{Osw} on behalf of Oswald ripening; (b) IA_{trans} representing transformation mechanism.

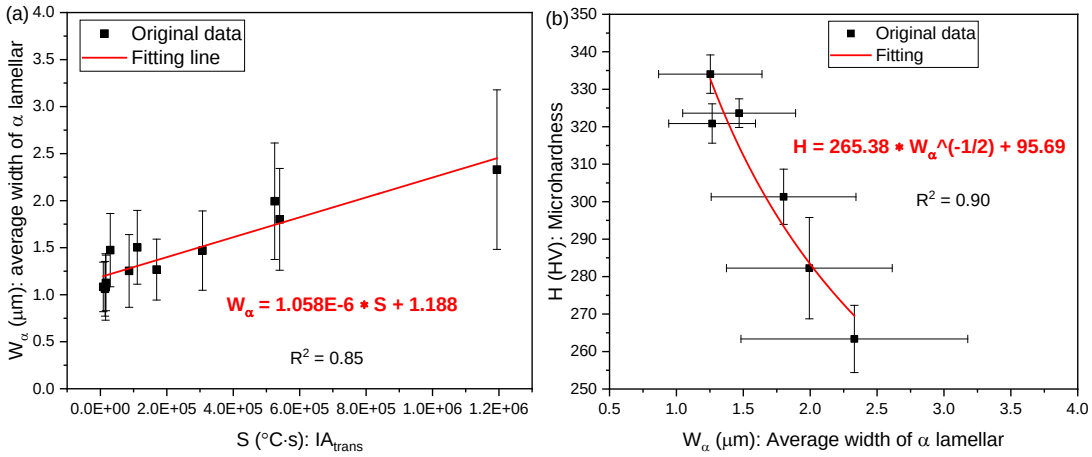

Figure 16. Relationship between the thermal history, the microstructure and the microhardness: (a) IA_{trans} vs. W_α; (b) H vs. W_α.